

## —Supporting information—

# Evaluating optimal $U$ for 3d transition-metal oxides within the SCAN+ $U$ framework

Olivia Y. Long,<sup>1</sup> Gopalakrishnan Sai Gautam,<sup>2</sup> Emily A. Carter<sup>2,3,\*</sup>

<sup>1</sup>Department of Physics, Princeton University, Princeton, NJ 08544, USA

<sup>2</sup>Department of Mechanical and Aerospace Engineering, Princeton University, Princeton, NJ 08544, USA

<sup>3</sup>Office of the Chancellor and Department of Chemical and Biomolecular Engineering, University of California, Los Angeles, Los Angeles, CA 90095-1405, USA

\*E-mail: eac@ucla.edu

## S1 Projector augmented-wave potentials

**Table S1:** Elements and their corresponding projector augmented-wave (PAW<sup>1</sup>) potentials used in our calculations. We used the “potPAW.52” set, which is designed for the Perdew-Burke-Ernzerhof functional<sup>2</sup> and contains information on the kinetic energy of the core electrons. The quoted text in the PAW potential column indicates the specific potential file that is available with the Vienna ab initio simulation package.<sup>3,4</sup> For example, “Cr\_pv” indicates “POTCAR.Cr\_pv.gz”. For each PAW potential, we also indicate the number of valence electrons treated self-consistently. In the case of copper, we used the “Cu\_pv” potential listed below in all our calculations except in **Figure S2** (see below), where we used both “Cu\_pv” and “Cu” potentials.

Element	PAW potential	Number of valence electrons
Oxygen	“O”	6
Scandium	“Sc_sv”	11
Titanium	“Ti_pv”	10
Vanadium	“V_pv”	11
Chromium	“Cr_pv”	12
Cobalt	“Co_pv”	15

Nickel	“Ni_pv”	16
Copper	“Cu_pv”	17
Zinc	“Zn”	12
Lithium	“Li”	1

## S2 Additional crystal structures

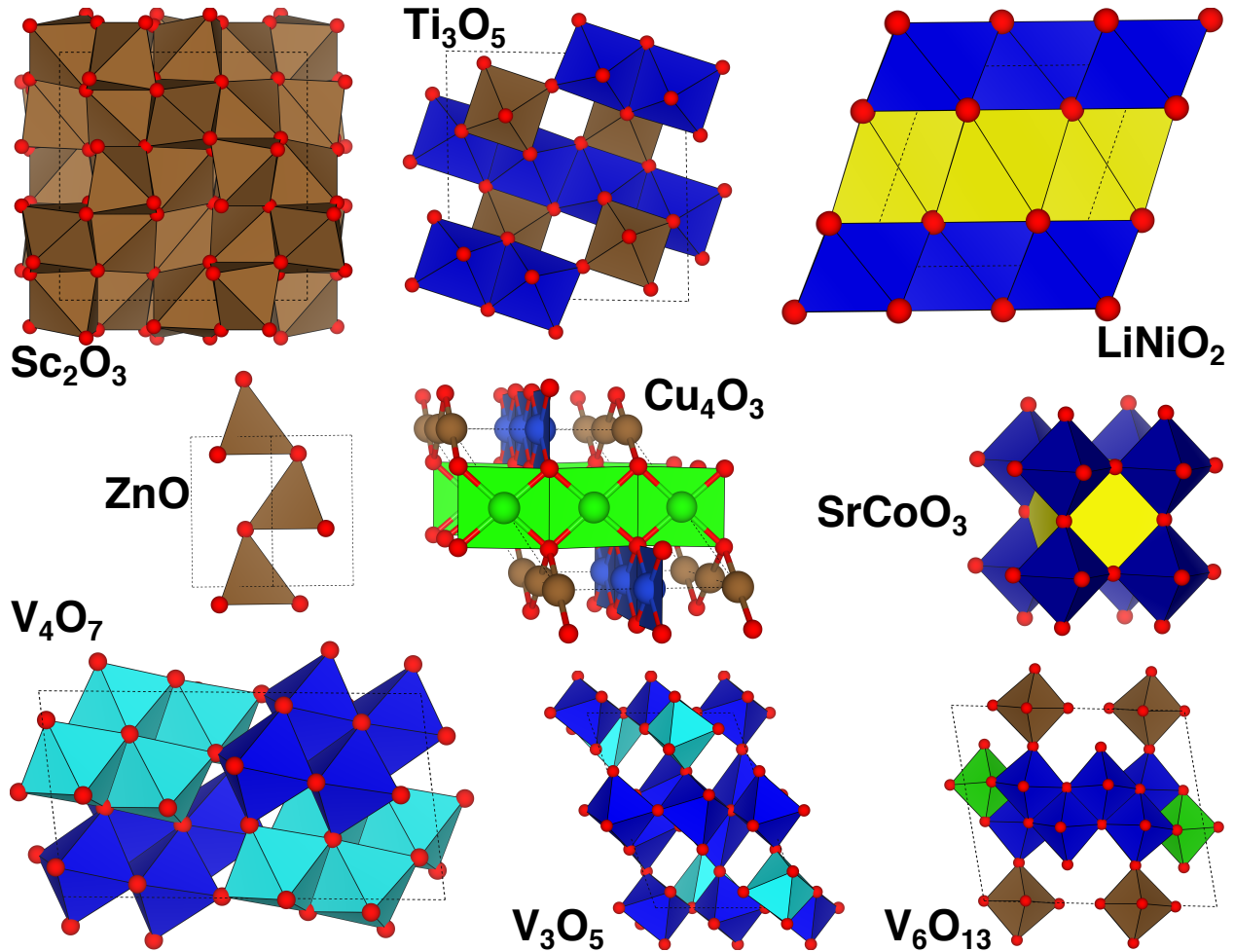


**Figure S1:** Initial crystal structures considered in evaluating the transferability of optimal U values determined for the various transition-metal systems. Dark blue and green polyhedra indicate atoms of identical oxidation states but with opposite magnetic spin. Brown polyhedra indicate metal atoms without any magnetic moment. In V<sub>4</sub>O<sub>7</sub> (space group:  $P2/c$ ) and V<sub>3</sub>O<sub>5</sub> ( $A\bar{1}$ ) the dark and light blue polyhedra respectively signify V atoms with lower and higher oxidation states. In the case of Ti<sub>3</sub>O<sub>5</sub> ( $C2/m$ ), Cu<sub>4</sub>O<sub>3</sub> ( $I4_1/amd$ ), and V<sub>6</sub>O<sub>13</sub> ( $C2/m$ ), the brown polyhedra represent Ti<sup>4+</sup>, Cu<sup>+</sup>, and V<sup>5+</sup>, while the yellow polyhedra in LiNiO<sub>2</sub> ( $C2/m$ ) and SrCoO<sub>3</sub> ( $Pm\bar{3}m$ ) show Li and Sr, respectively. The initial structure of NiO<sub>2</sub> ( $C2/m$ , see **Figure S7**) is obtained by removing the Li atoms of the LiNiO<sub>2</sub> ( $C2/m$ ) structure shown here. The space groups of Sc<sub>2</sub>O<sub>3</sub> and ZnO are  $Ia\bar{3}$  and  $P6_3mc$ , respectively.

### S3 Effect of including outer-core states of Cu

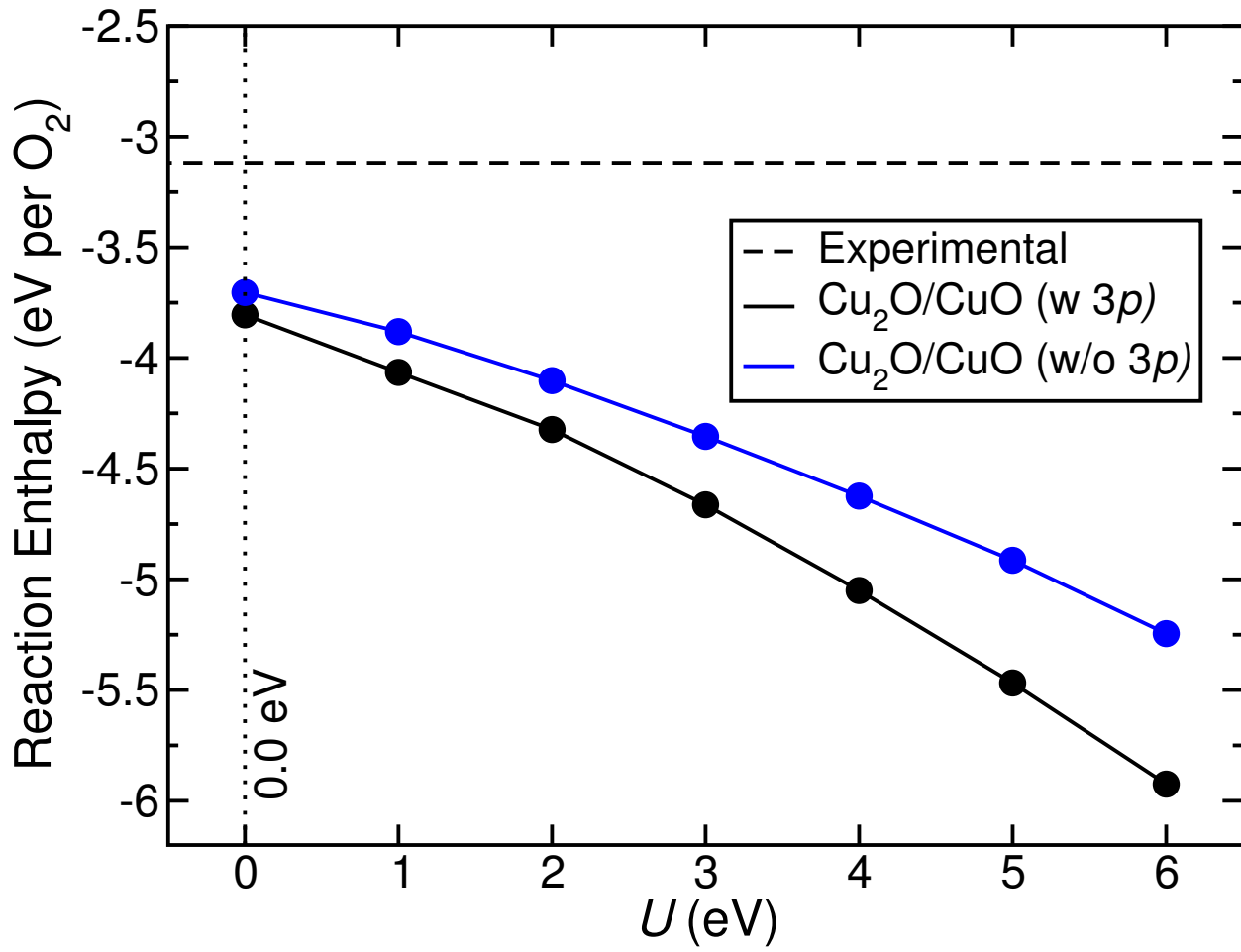


**Figure S2:** Variation of the  $2\text{Cu}_2\text{O} + \text{O}_2 \rightarrow 4\text{CuO}$  reaction enthalpy with increasing magnitude of  $U$  within the SCAN+ $U$  framework. Blue circles and the blue solid line indicate calculations without considering the  $3p$  outer-core states of Cu self-consistently, while black circles and the black solid line correspond to the  $3p$  electrons being treated self-consistently. Dashed black line is the experimental reaction enthalpy and the dotted black line indicates the optimal  $U$  ( $= 0.0$  eV).

## S4 Electronic structure of titanium oxides

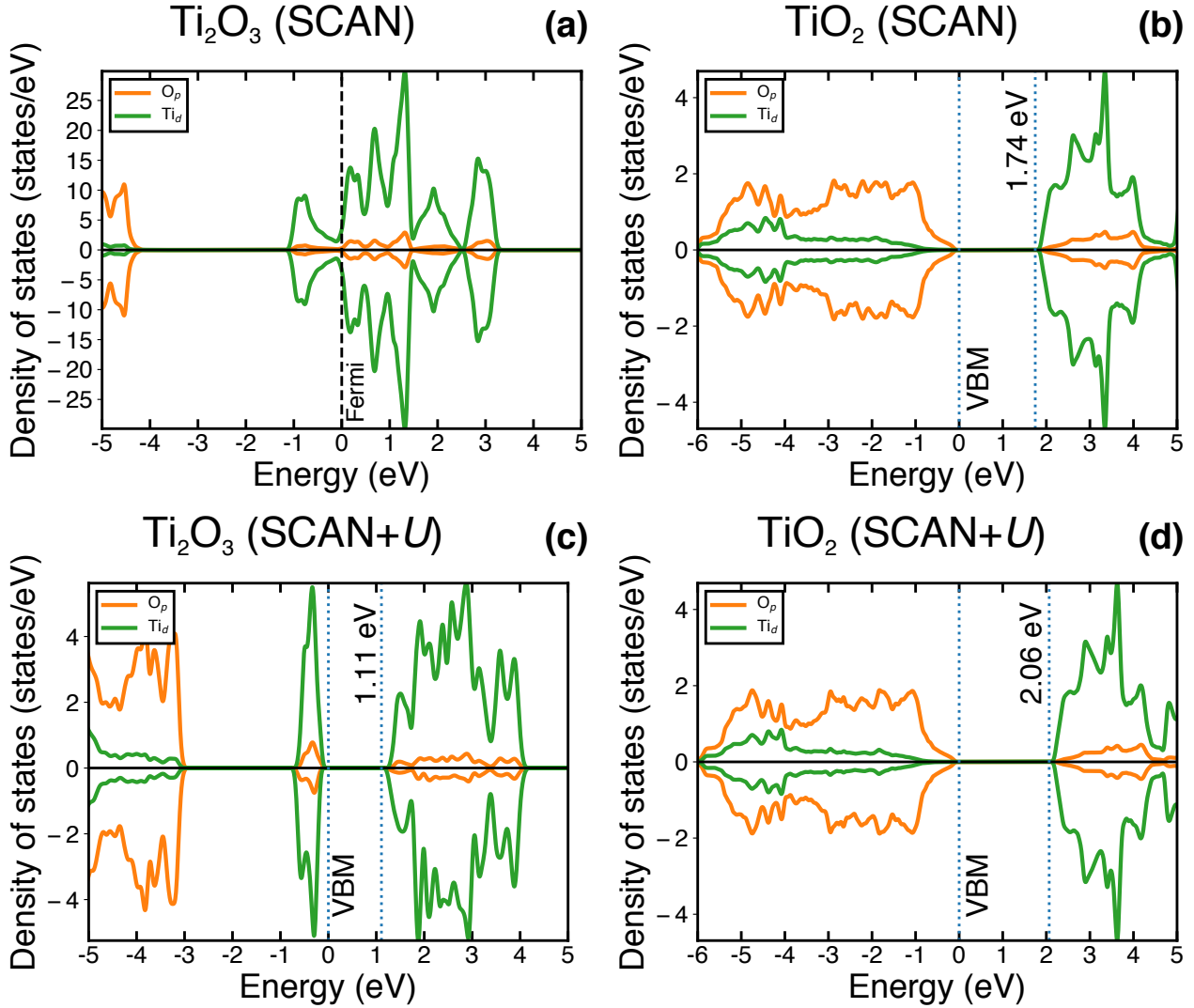


**Figure S3:** Densities of states (DOS) for the ground-state antiferromagnetic configuration of  $\text{Ti}_2\text{O}_3$  (panels a and c) and non-magnetic rutile- $\text{TiO}_2$  (panels b and d) calculated using DFT-SCAN (panels a and b) and  $\text{SCAN}+U_{\text{Ti}}$  ( $U_{\text{Ti}} = 2.5 \text{ eV}$ , panels c and d). Orange and green lines correspond to  $\text{O} 2p$  and  $\text{Ti} 3d$  states. Dashed black lines are Fermi levels in metallic system(s) while dotted blue lines are valence and conduction band edges for non-metallic system(s). The zero on the energy scale is set to either the Fermi level (metallic systems) or the valence band maximum (VBM, non-metallic systems). For structure(s) with a band gap, the value of the gap is indicated by the text annotation at the conduction band edge. States/eV below zero are minority spin and states/eV above zero are majority spin.

## S5 Electronic structure of vanadium oxides

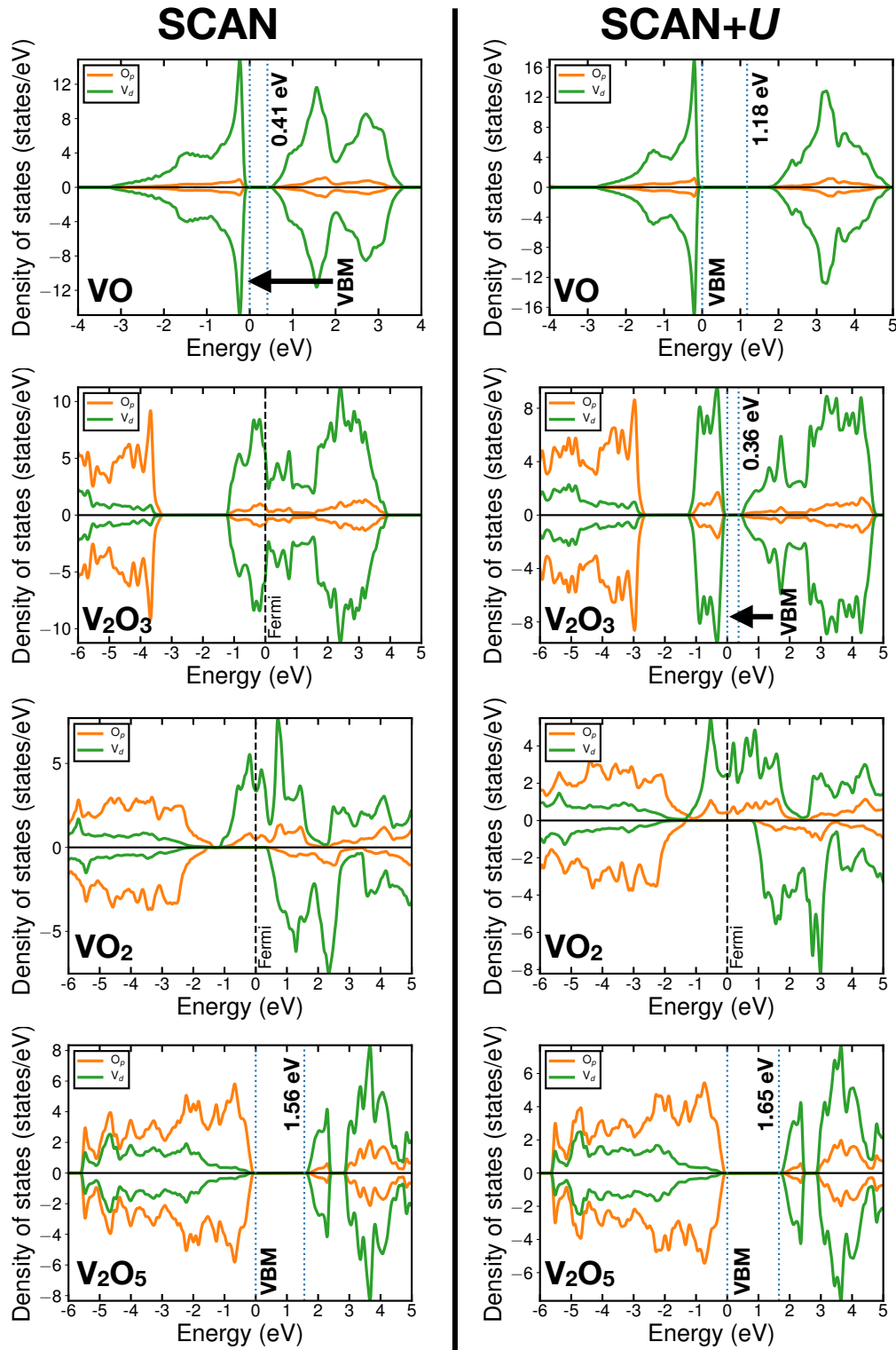


**Figure S4:** DOS for the ground-state magnetic configurations of VO (top row),  $V_2O_3$  (second row),  $VO_2$  (third row), and  $V_2O_5$  (bottom row) as calculated by DFT-SCAN (left column) and SCAN+ $U_V = 1.0$  eV (right column). Notations used within each panel are identical to **Figure S3**.

## S6 Electronic structure of chromium oxides

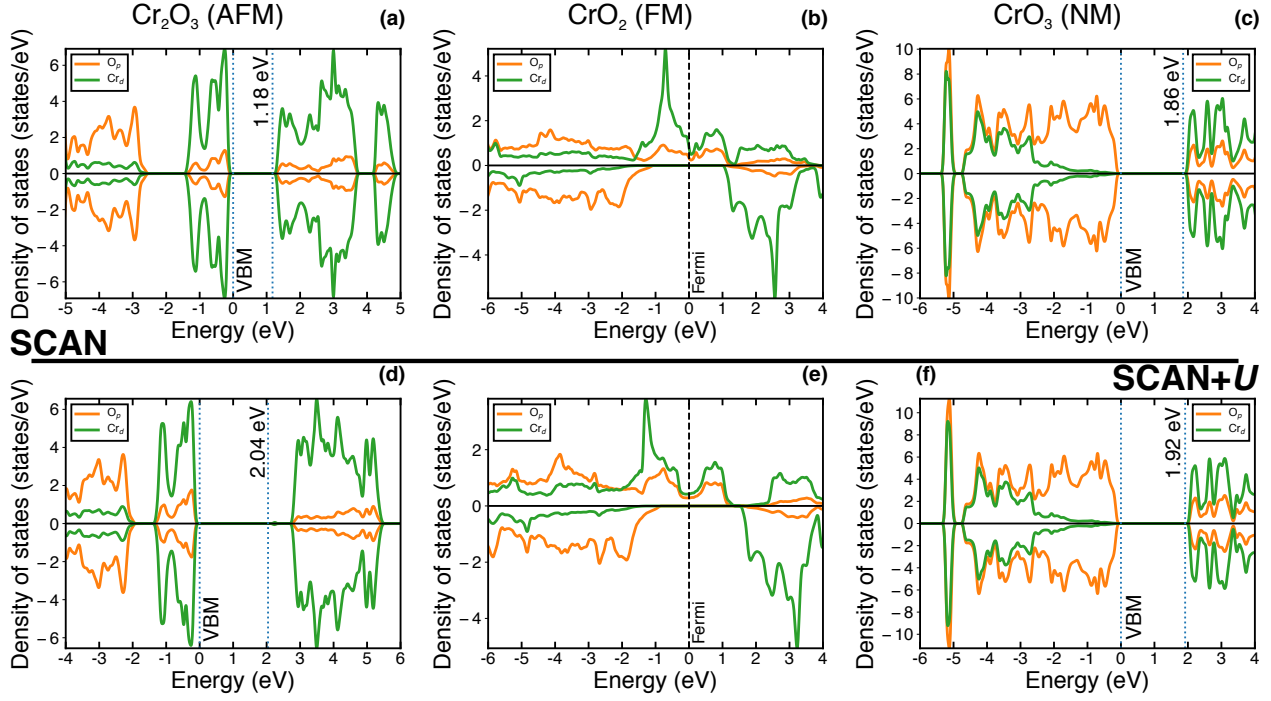


**Figure S5:** DOS for the ground-state magnetic configurations of Cr<sub>2</sub>O<sub>3</sub> (panels a, d), CrO<sub>2</sub> (b, e), and CrO<sub>3</sub> (c,f) as calculated by DFT-SCAN (panels a – c) and SCAN+U for  $U = 0.5$  eV (panels d – f). Notations used within each panel are identical to **Figure S3**.

**Figure S5** shows the DOS plotted for ground-state magnetic configurations of Cr<sub>2</sub>O<sub>3</sub>, CrO<sub>2</sub>, and CrO<sub>3</sub> for DFT-SCAN and SCAN+U ( $U = 0.5$  eV). DFT-SCAN and SCAN+U predict qualitatively similar behavior for all Cr oxides considered, highlighting that a  $U$  correction is not required for accurately modeling Cr oxides with SCAN. For example, DFT-SCAN and SCAN+U both rightly yield half-metallic behavior in rutile-CrO<sub>2</sub> (**Figure S5b** and **e**), signified by the metallic and insulating behaviors of the majority (DOS above zero) and minority (DOS below zero) spin channels, respectively, in agreement with experiments.<sup>5</sup> Importantly, CrO<sub>2</sub> is the only thermodynamically stable MO<sub>2</sub> oxide (M = 3d metal) which remains (half) metallic under sub-298 K conditions.<sup>5</sup> Additionally, DFT-SCAN and SCAN+U both predict similarly insulating behavior for CrO<sub>3</sub> (band gaps of 1.86 and 1.92 eV, panels c and f in **Figure S5**), in qualitative agreement with experiments (band gap  $\sim 3.80$  eV<sup>6</sup>). Also, the charge-transfer behavior of CrO<sub>3</sub>, highlighted by O 2p states (orange lines) at the VBM and Cr 3d states (green lines) at the CBM is captured equally well by DFT-SCAN and SCAN+U. Significantly, DFT-SCAN and SCAN+U's predicted band gaps in Cr<sub>2</sub>O<sub>3</sub>

differ by  $\sim 0.86$  eV (**Figure S5a** and **d**), although both frameworks produce insulating behavior, in qualitative agreement with experiments (band gap  $\sim 3.2$  eV<sup>7</sup>). The deviation in DFT-SCAN versus SCAN+ $U$  band gaps can be attributed to the presence of the highest number of unpaired  $d$  electrons on each Cr ion in  $\text{Cr}_2\text{O}_3$  (three) among the Cr oxides considered and hence this oxide is impacted most by the addition of  $U$ .

## S7 Electronic structure of $\text{Co}_3\text{O}_4$ and $\text{CoO}_2$

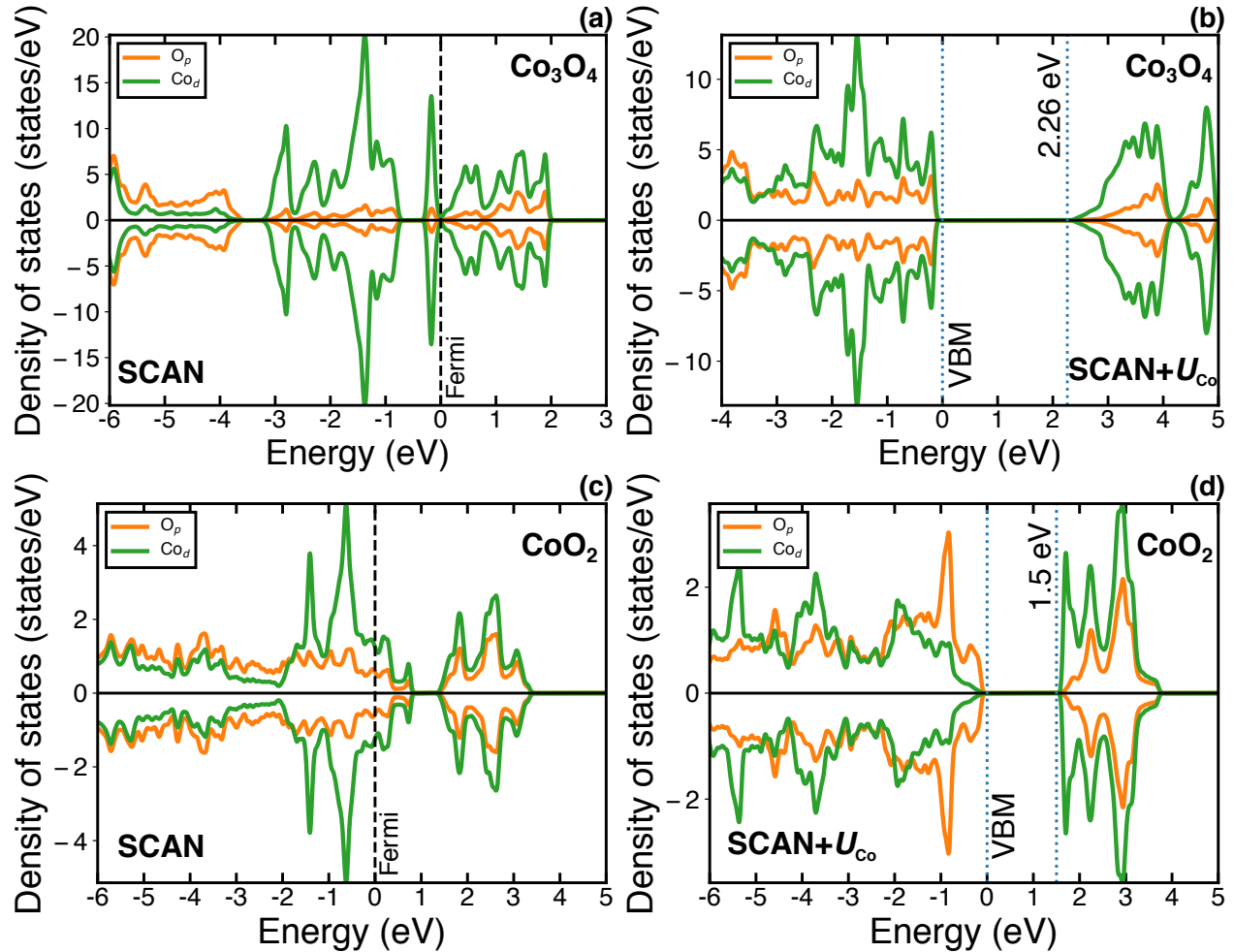


**Figure S6:** DOS for the ground-state magnetic configuration of spinel- $\text{Co}_3\text{O}_4$  (panels a and b) and antiferromagnetic O1- $\text{CoO}_2$  (panels c and d) as calculated by DFT-SCAN (panels a and c) and SCAN+ $U_{\text{Co}}$  for  $U_{\text{Co}} = 3.0$  eV (panels b and d). Notations used within each panel are identical to **Figure S3**.

## S8 Electronic structure of nickel oxides

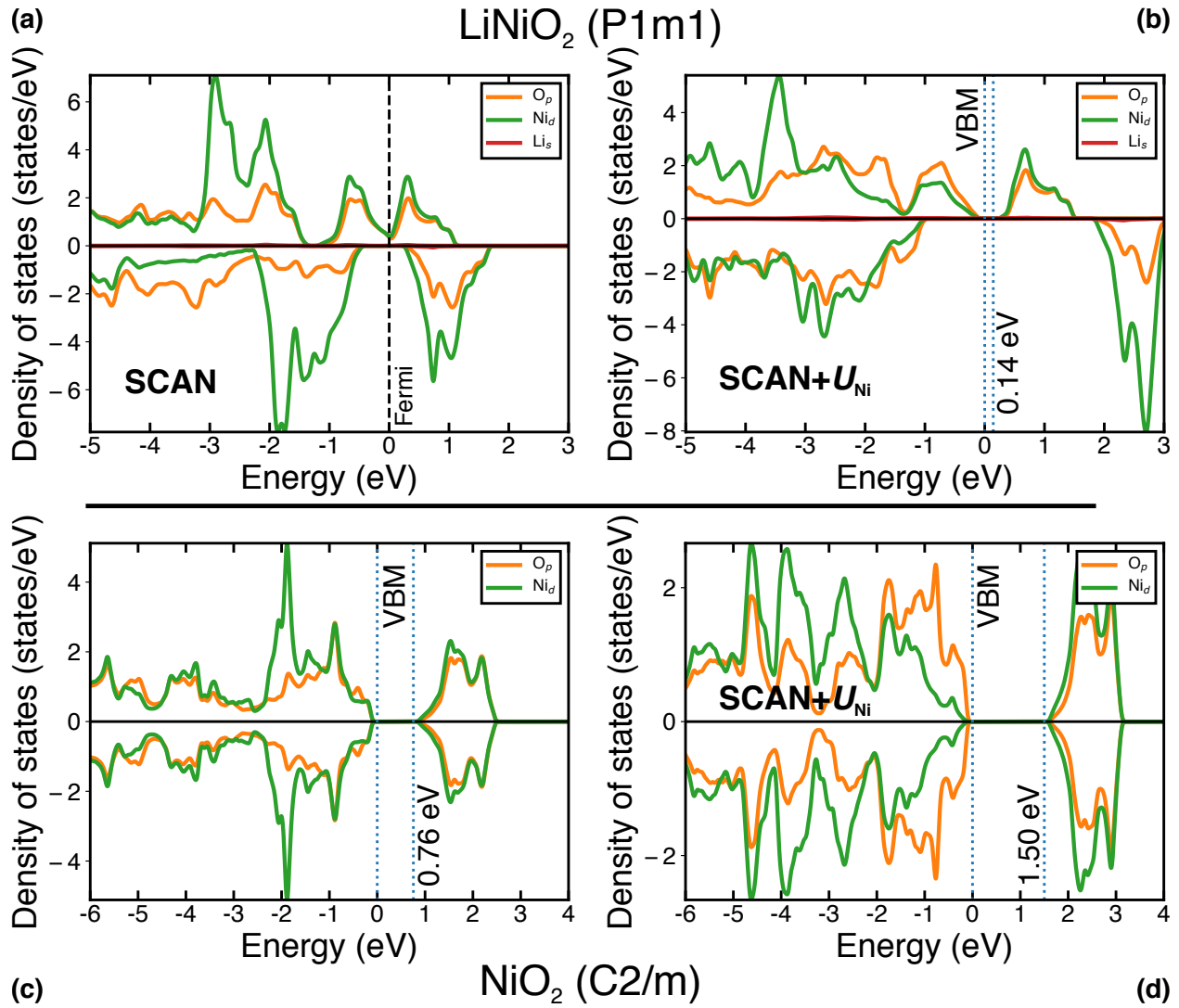


**Figure S7:** DOS for the ferromagnetic LiNiO<sub>2</sub> (panels a and b) and NiO<sub>2</sub> (panels c and d), as calculated by DFT-SCAN (left column) and SCAN+ $U_{\text{Ni}}$  (right column) for  $U_{\text{Ni}} = 2.5$  eV. The LiNiO<sub>2</sub> polymorph considered here was used to obtain the  $U_{\text{Ni}}$  value (**Figure 2e** in the main text) and is different from the one considered in **Figure S11**. The initial structure of NiO<sub>2</sub> was obtained by removing the Li atoms from the LiNiO<sub>2</sub> structure shown in **Figure S1**. Notations used within each panel are identical to **Figure S3**.

**S9 Crystal structures of anatase and brookite  $\text{TiO}_2$**

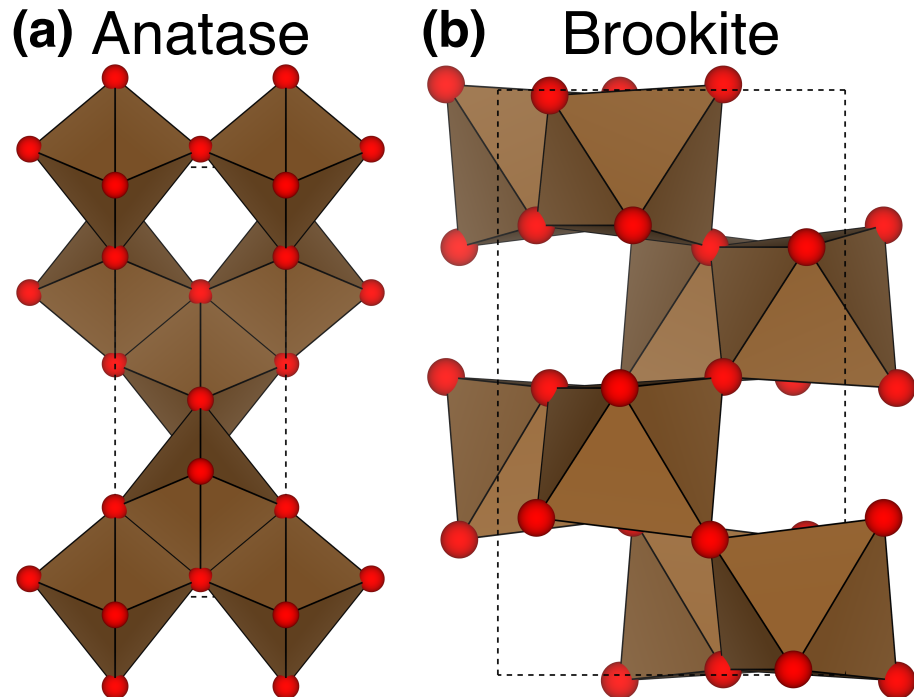


**Figure S8:** Unit cells of anatase (space group:  $I4_1/\text{amd}$ ) and brookite ( $Pbca$ )  $\text{TiO}_2$ . Red spheres represent oxygen, brown polyhedra titanium.

## S10 Antiferromagnetic configurations in zinc blende CoO

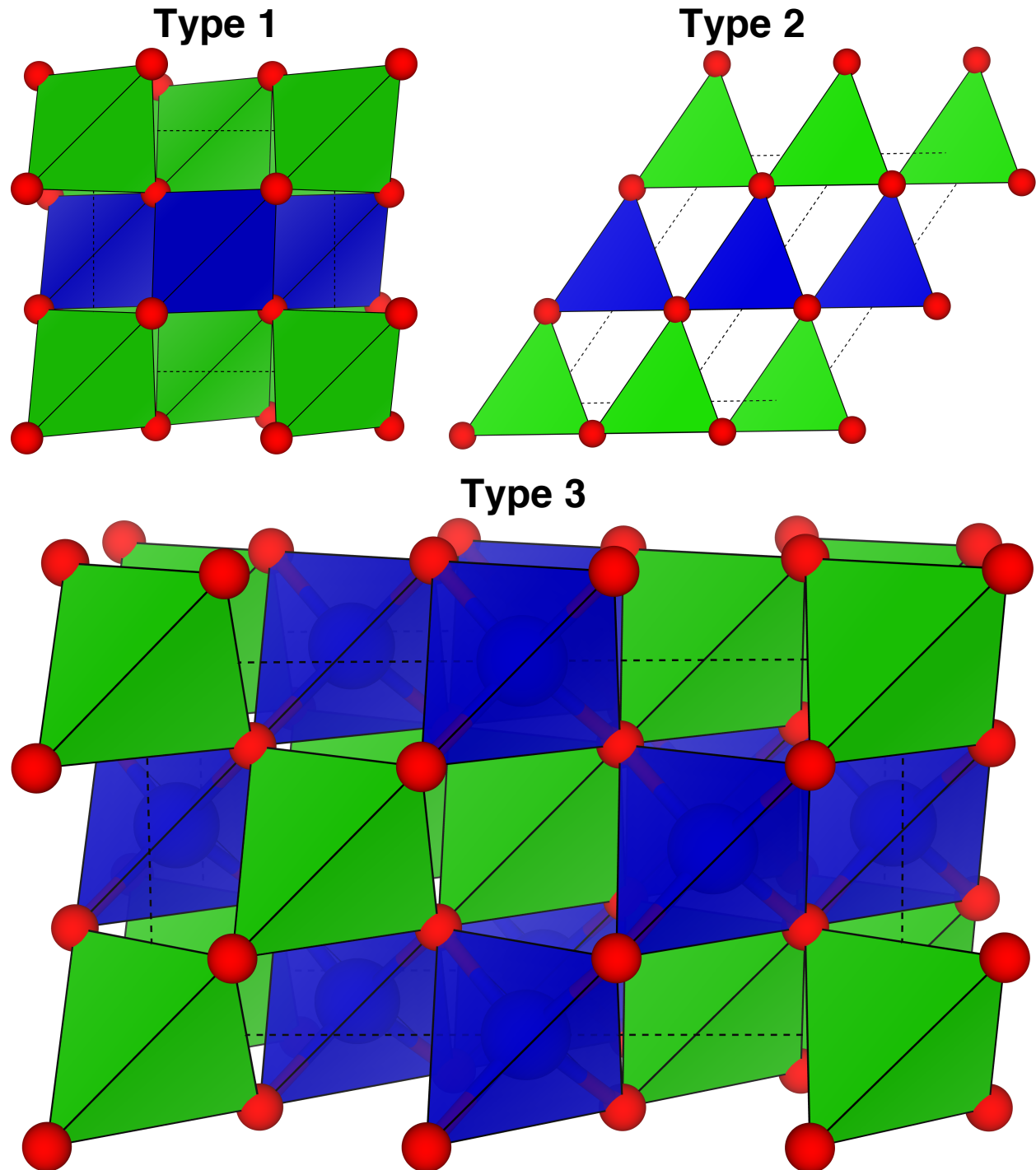


**Figure S9:** Three common types of antiferromagnetic configurations possible in zinc blende (space group:  $F\bar{4}3m$ ) CoO. Red spheres indicate oxygen. Green and blue polyhedra represent Co atoms with opposite magnetic moments.

## S11 Transferability checks in cobalt oxides: SrCoO<sub>3</sub> and CoO<sub>2</sub>

**Table S2:** Lattice parameters and magnetic moments (on Co atom) in the primitive cell of cubic SrCoO<sub>3</sub>. We attempted three different initializations of the magnetic moment, namely 5 (signifying high-spin Co<sup>4+</sup>), 3 (intermediate-spin), and 1 (low-spin). Both DFT-SCAN and SCAN+ $U_{\text{Co}}$  always converged to the intermediate-spin state for the Co atom during structure relaxation.

Source	Lattice constants (Å)			Lattice vector angles (°)			$M$ ( $\mu_{\text{B}}$ )	
	$a$	$b$	$c$	$\alpha$	$\beta$	$\gamma$	Initial	Relaxed
Expt.	3.86			90.0			2.5	
DFT-SCAN	3.79			90.0			5	2.05
							3	
							1	
SCAN+ $U_{\text{Co}}$	3.82			90.0			5	2.91
							3	
							1	

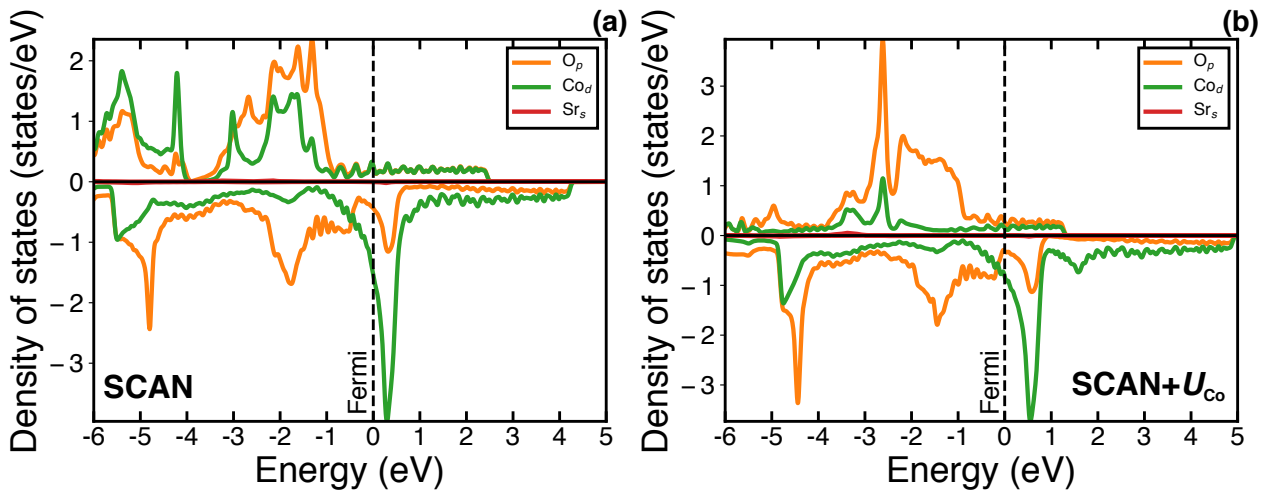


**Figure S8:** DOS for ferromagnetic, cubic-SrCoO<sub>3</sub> as calculated by DFT-SCAN (panel a) and SCAN+ $U_{\text{Co}}$  for  $U_{\text{Co}} = 3.0$  eV (panel b). Notations used within each panel are identical to **Figure S3**.

**Table S3:** Lattice parameters in ferromagnetic and antiferromagnetic O1-CoO<sub>2</sub> and ferromagnetic O3-CoO<sub>2</sub>, as calculated using DFT-SCAN and SCAN+ $U_{\text{Co}}$  ( $U_{\text{Co}} = 3.0$  eV). Alternate Co layers along the  $c$ -axis were aligned with opposite spins to model the antiferromagnetic O1-CoO<sub>2</sub> structure, resulting in the use of a  $1 \times 1 \times 2$  supercell compared to using just the unit cell for the ferromagnetic configuration. No experimental lattice parameters are available for the O3-CoO<sub>2</sub> structure as it is identical to O3-LiCoO<sub>2</sub> with all the Li atoms removed.

Compound	Source	Lattice constants (Å)			Lattice vector angles (°)		
		$a$	$b$	$c$	$\alpha$	$\beta$	$\gamma$
O1-CoO <sub>2</sub> (Ferromagnetic)	Expt.	2.82		4.24	90.0	120.0	
	DFT-SCAN	2.78		4.35			
	SCAN+ $U_{\text{Co}}$	2.80		4.49			
O1-CoO <sub>2</sub> (Antiferromagnetic)	Expt.	2.82		8.48	90.0	120.0	
	DFT-SCAN	2.78		8.71			
	SCAN+ $U_{\text{Co}}$	2.80		8.76			
O3-CoO <sub>2</sub> (Ferromagnetic)	Expt.	N/A					
	DFT-SCAN	2.78		13.34	90.0	120.0	
	SCAN+ $U_{\text{Co}}$	2.80		13.50			

## S12 Transferability checks in nickel oxides: LiNiO<sub>2</sub> and NiCr<sub>2</sub>O<sub>4</sub>

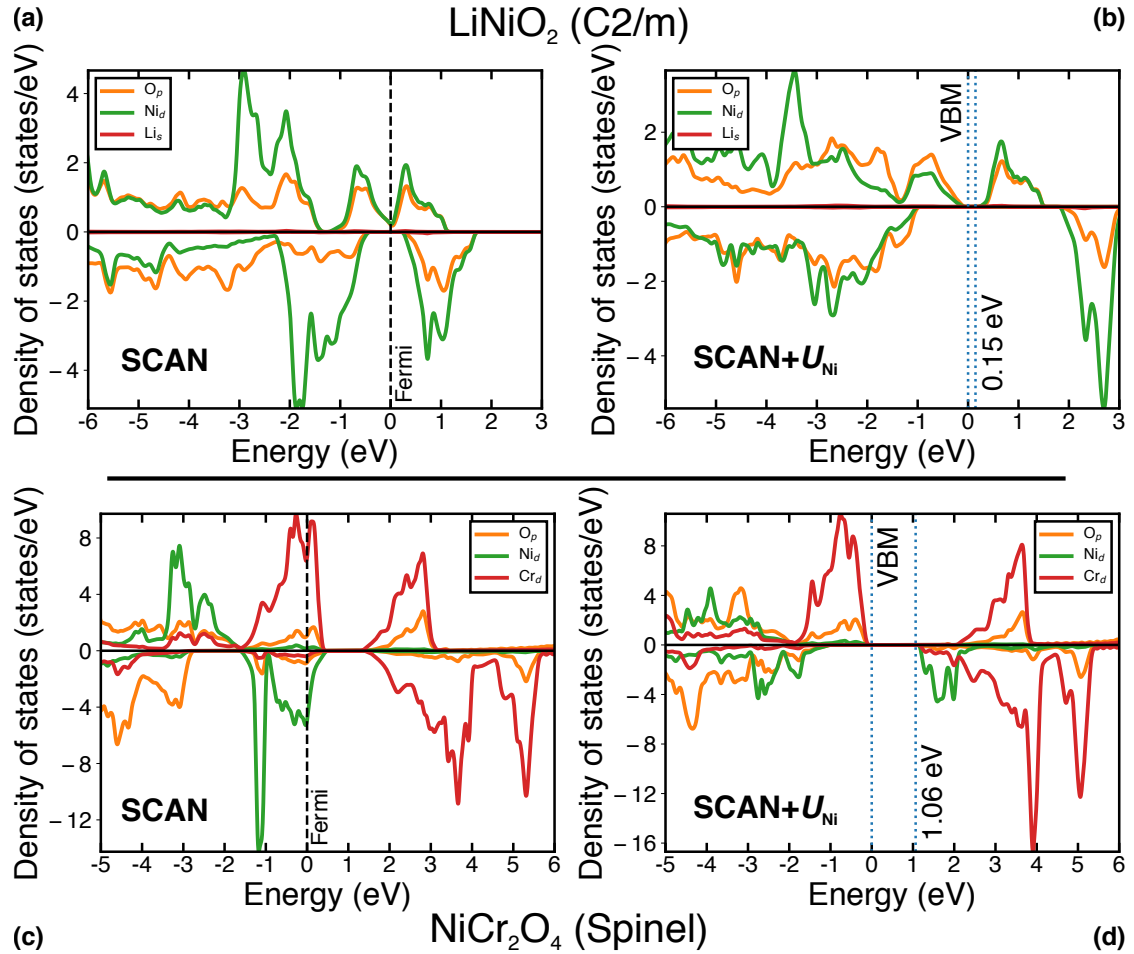


**Figure S9:** DOS for (a, b) LiNiO<sub>2</sub> (space group: *C2/m*) and (c, d) spinel-NiCr<sub>2</sub>O<sub>4</sub> as predicted by DFT-SCAN and SCAN+ $U_{\text{Ni}}$ , where  $U_{\text{Ni}} = 2.5$  eV. Orange and green lines correspond to O *p* and Ni *d* states, while the red lines indicate Li 2s states in panels (a, b) and Cr 3d states in panels (c, d). Notations used in the figure are similar to Figure S3.

To test the transferability of the optimal  $U_{\text{Ni}} = 2.5$  eV, we applied the correction to monoclinic LiNiO<sub>2</sub> with the C2/m space group (**Figure S1**) and to spinel-NiCr<sub>2</sub>O<sub>4</sub>. Note that the LiNiO<sub>2</sub> structure considered here is different from the P1m1 structure of **Figure 1** of the main text because an accurate band gap (at the G<sub>0</sub>W<sub>0</sub>@GGA+*U* level<sup>8</sup>) was calculated only for the C2/m polymorph whereas band gap measurements do not exist yet for LiNiO<sub>2</sub>. In the case of NiCr<sub>2</sub>O<sub>4</sub> (structure similar to Co<sub>3</sub>O<sub>4</sub> in **Figure 1**), where the Ni<sup>2+</sup> and Cr<sup>3+</sup> ions occupy respectively the tetrahedral and octahedral sites, band gap measurements are available for the FM structure that is stable under ambient conditions.<sup>9</sup> Thus, **Figure S11** plots the DOS predicted by DFT-SCAN (panels a and c) and SCAN+ $U_{\text{Ni}}$  (panels b and d) for LiNiO<sub>2</sub> (panels a and b) and NiCr<sub>2</sub>O<sub>4</sub>

(panels c and d). In the case of  $\text{LiNiO}_2$ , DFT-SCAN incorrectly predicts half-metallic behavior, while SCAN+ $U_{\text{Ni}}$  predicts a band gap of  $\sim 0.15$  eV, qualitatively consistent with the  $\text{G}_0\text{W}_0@\text{GGA}+U$  prediction (band gap  $\sim 0.96$  eV<sup>8</sup>). Similarly, for  $\text{NiCr}_2\text{O}_4$ , SCAN+ $U_{\text{Ni}}$  is in better agreement with experiments (measured band gap  $\sim 1.7$  eV<sup>10</sup>) with its predicted  $\sim 1.06$  eV band gap compared to DFT-SCAN's metallic prediction. DOS calculations via DFT-SCAN and SCAN+ $U_{\text{Ni}}$  in binary, metastable  $\text{NiO}_2$  (space group: C2/m), also show similar trends of a larger gap with the latter (**Figure S7**). Thus, our transferability checks with  $\text{LiNiO}_2$  and  $\text{NiCr}_2\text{O}_4$  confirm that the  $U_{\text{Ni}}$  correction (in SCAN+ $U$ ) is necessary to describe accurately the electronic structure of Ni oxides.

### S13 Transferability check in copper oxides: $\text{Cu}_4\text{O}_3$

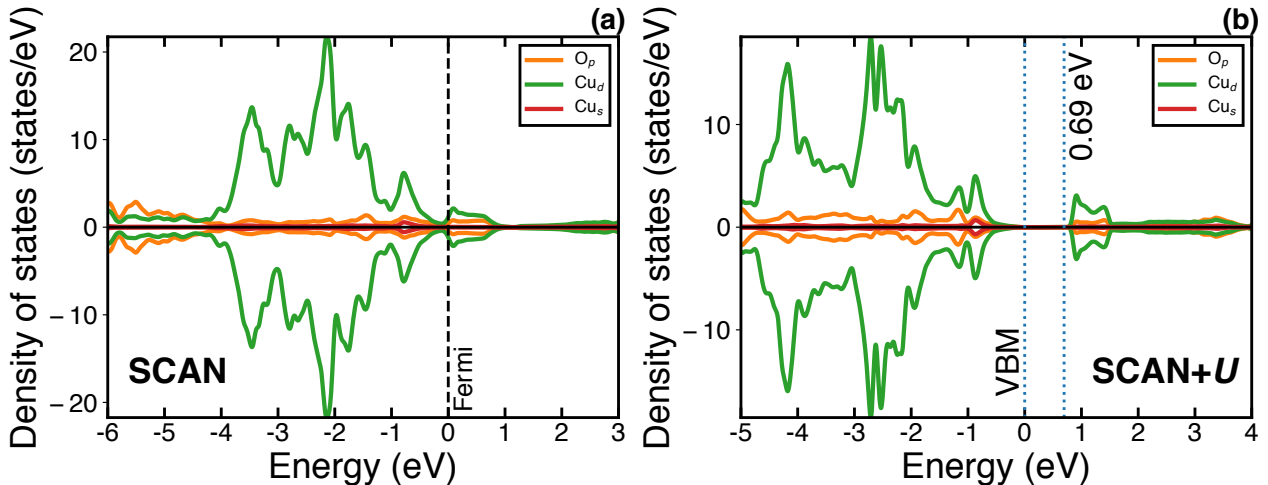


**Figure S10:** DOS for  $\text{Cu}_4\text{O}_3$  calculated by (a) DFT-SCAN and (b) SCAN+ $U$ , where  $U = 2$  eV. Orange, green, and red lines correspond to O 2p, Cu 3d, and Cu 4s states. Notations within each panel are similar to **Figure S3**.

Finally, we tested the effect of including a  $U$  correction on  $\text{Cu}_4\text{O}_3$  for copper oxides. Note that we used  $U = 2$  eV here, since there is no need for a  $U$  correction based on the oxidation enthalpy of  $\text{Cu}_2\text{O} \rightarrow \text{CuO}$  (**Figure 2f** of the main text).  $\text{Cu}_4\text{O}_3$  exhibits mixed oxidation states of +1/+2 and adopts an AFM, tetragonal configuration in its ground state,<sup>11</sup> and is known to be a semiconductor with a band gap of  $\sim 1.34$  eV.<sup>12</sup> Due to the large size of the AFM unit cell of  $\text{Cu}_4\text{O}_3$  (a  $2 \times 2 \times 2$  supercell of the primitive cell<sup>11</sup>), we only considered the AFM configurations possible within the primitive cell (14 atoms) to reduce computational cost, similar to Ref.<sup>13</sup>. **Figure S12** plots the DOS for  $\text{Cu}_4\text{O}_3$  in its most stable AFM configuration (structure

shown in **Figure S1**), as predicted by DFT-SCAN (panel a) and SCAN+*U* (panel b). Similar to trends observed in CuO (**Figure 7** of the main text), DFT-SCAN incorrectly predicts metallic behavior in Cu<sub>4</sub>O<sub>3</sub> whereas SCAN+*U* predicts a 0.69 eV band gap. Thus, although adding a *U* correction worsens predictions of redox thermodynamics in Cu oxides, including the *U* will be essential to model the electronic behavior (and related properties).

## S14 Calculated formation energies of Sc<sub>2</sub>O<sub>3</sub> and ZnO

**Table S4:** Formation energy of Sc<sub>2</sub>O<sub>3</sub> and ZnO (eV/O<sub>2</sub>), as calculated by DFT-SCAN.

<b>Compound (space group)</b>	<b>Reaction</b>	<b>Formation energy (eV/O<sub>2</sub>)</b>	
		<b>Expt.</b>	<b>DFT-SCAN</b>
Sc <sub>2</sub> O <sub>3</sub> (Ia $\bar{3}$ )	$\frac{4}{3} \text{ Sc} + \text{O}_2 \rightarrow \frac{2}{3} \text{ Sc}_2\text{O}_3$	-13.18	-13.09
ZnO ( <i>P</i> 6 <sub>3</sub> <i>mc</i> )	2 Zn + O <sub>2</sub> → 2 ZnO	-7.22	-6.63

## References

- <sup>1</sup> G. Kresse and D. Joubert, Phys. Rev. B **59**, 1758 (1999).
- <sup>2</sup> J.P. Perdew, K. Burke, and M. Ernzerhof, Phys. Rev. Lett. **77**, 3865 (1996).
- <sup>3</sup> G. Kresse and J. Hafner, Phys. Rev. B **47**, 558 (1993).
- <sup>4</sup> G. Kresse and J. Furthmüller, Phys. Rev. B **54**, 11169 (1996).
- <sup>5</sup> J.M.D. Coey and M. Venkatesan, J. Appl. Phys. **91**, 8345 (2002).
- <sup>6</sup> R.H. Misho, W.A. Murad, and G.H. Fattahallah, Thin Solid Films **169**, 235 (1989).
- <sup>7</sup> M.M. Abdullah, F.M. Rajab, and S.M. Al-Abbas, AIP Adv. **4**, 027121 (2014).
- <sup>8</sup> D.-H. Seo, A. Urban, and G. Ceder, Phys. Rev. B **92**, 115118 (2015).
- <sup>9</sup> M. Reehuis, M. Tovar, D.M. Többens, P. Pattison, A. Hoser, and B. Lake, Phys. Rev. B **91**, 024407 (2015).
- <sup>10</sup> M. Enhessari, A. Salehabadi, S. Khanahmadzadeh, K. Arkat, and J. Nouri, High Temp. Mater. Process. **36**, (2017).
- <sup>11</sup> M.-H. Whangbo and H.-J. Koo, Inorg. Chem. **41**, 3570 (2002).
- <sup>12</sup> J.F. Pierson, A. Thobor-Keck, and A. Billard, Appl. Surf. Sci. **210**, 359 (2003).
- <sup>13</sup> M. Heinemann, B. Eifert, and C. Heiliger, Phys. Rev. B **87**, 115111 (2013).